发 光 学 报
CHINESE JOURNAL OF LUMINESCENCE

Article ID: 1000-7032(XXXX)XX-0001-14

Interfacial engineering of perovskite/PCBM heterojunctions with macrocyclic calixarene for inverted perovskite solar cells

YANG Xue-ke[1], HE Zhen[1*], PU Yuan-wei[2], LIANG Yong-chao[2], ZHAO Feng-gui[1], ZUO Ying-qi[1], WANG Chu-ying[1], XIONG Jian[1*]

(1. *Engineering Research Center of Electronic Information Materials and Devices (Ministry of Education), Guangxi Key Laboratory of Information Materials, School of Materials Science and Engineering, Guilin University of Electronic and Technology, Guilin* 541004, *China.*;
2. *School of Big Data and Information Engineering, Guizhou University, Guiyang* 550025, *P. R. China.*)
* *Corresponding Authors, E-mail: hzhfree*@163.*com*; *xiongjiankyxx*@163.*com*

Abstract: Performance and stability of inverted perovskite solar cells (PSCs) are severely constrained by non-radiative recombination induced by defect accumulation and inferior interfacial contact at the perovskite/[6,6]-phenyl-C_{61}-butyric acid methyl ester (PCBM) heterojunction. Herein, a multifunctional interfacial modification strategy employing 4-sulfocalix[6]arene (SC6A) is developed to resolve the inherent interfacial drawbacks of the PVSK/PCBM interface. As a calixarene derivative, SC6A features a cup-shaped macrocyclic aromatic skeletons functionalized with abundant sulfonic (-SO_3H) and hydroxyl (-OH) groups. It affords multi-site and omnidirectional coverage on perovskite surface, synchronously passivating diverse defects and restraining carrier non-radiative recombination. Its unique cavity can form π - π interactions with PCBM, which helps regulate the distribution of PCBM molecules and improve their dispersion. This ameliorates the uniformity of the PCBM film, optimizes the inferior interfacial contact, and further facilitates charge carrier transport efficiency. Benefiting from these synergistic effects, the resultant SC6A-modified device achieves a high-power conversion efficiency (PCE) of 24.56%. Furthermore, the SC6A-based device exhibits excellent stability, retaining 93% of its initial PCE after 1500 h of storage in N_2 atmosphere and 80% after 500 h of thermal aging at 65°C, outperforming the unmodified control device significantly.

Keywords: 4-Sulfocalix[6]arene; Interfacial modification; Inverted perovskite solar cells
CLC number: **Document code**:
DOI: 10.3724/CJL.20260243 **CSTR**: 32170.14.CJL.20260243

基于大环杯芳烃的钙钛矿/PCBM异质结界面工程及其在倒置钙钛矿太阳能电池中的应用

杨雪珂[1], 何 珍[1*], 蒲元伟[2], 梁永超[2], 赵丰贵[1], 左颖淇[1], 王楚滢[1], 熊 健[1*]

(1.桂林电子科技大学材料科学与工程学院, 电子信息材料与器件教育部工程研究中心, 广西信息材料重点实验室, 广西 桂林 541004;
2.贵州大学大数据与信息工程学院, 贵州 贵阳 550025)

收稿日期: XXXX-XX-XX; **修订日期**: XXXX-XX-XX
基金项目: 国家自然科学基金(62264004);广西自然科学基金(2026GXNSFDA00640025);桂林电子科技大学博士科研启动基金资助项目(UF15016Y)
Supported by National Natural Science Foundation of China(62264004); Guangxi Natural Science Foundation (2026GXNSFDA00640025);Ph.D. Research Startup Foundation of Guilin University of Electronic Technology(UF15016Y)

摘要：倒置钙钛矿太阳能电池(PSCs)的性能和稳定性严重受限于钙钛矿/[6,6]-苯基-C_{61}-丁酸甲酯(PCBM)异质结处缺陷积累和不良界面接触所引发的非辐射复合。本文提出了一种基于4-磺酰杯[6]芳烃(SC6A)的多功能界面修饰策略,用以解决PVSK/PCBM界面固有的缺陷问题。作为杯芳烃衍生物,SC6A具有杯状大环芳香骨架,并带有丰富的磺酸基团(-SO_3H)和羟基基团(-OH)。它能够在钙钛矿表面实现多位点、全方位的覆盖,同步钝化多种缺陷并抑制载流子的非辐射复合。其独特的空腔结构能与PCBM形成π-π相互作用,有助于调控PCBM分子的分布并改善其分散性。这改善了PCBM薄膜的均匀性,优化了不良的界面接触,并进一步促进了载流子传输效率。得益于这些协同效应,经SC6A修饰的器件实现了24.56%的高功率转换效率(PCE)。此外,基于SC6A的器件表现出优异的稳定性,在N_2气氛下储存1500小时后仍保持初始PCE的93%,在65°C下热老化500小时后仍保持80%,显著优于未修饰的对照器件。

关 键 词：4-磺酰杯[6]芳烃；界面修饰；倒置钙钛矿太阳能电池

1 Introduction

Growing global demand for renewable energy establishes solar photovoltaics as a key energy solution[1-2]. Organic-inorganic hybrid halide perovskites offer great promise as solar-harvesting materials applied in photovoltaics due to their cost-effective fabrication process, long charge carrier lifetime, tunable band gap, and high absorption coefficient[3-4]. Inverted perovskite solar cells (PSCs) exhibit distinct advantages, including solution processability, negligible hysteresis, and easy integration with tandem devices, making them promising for commercial applications[5]. In inverted PSCs, the electron transporting layer (ETL) plays a vital role in carrier extraction and transmission, and defect passivation and stabilization of the perovskite layer, significantly influencing the device performance[6-7]. Currently, fullerene derivative [6,6]-phenyl-C61-butyric acid methyl ester (PCBM) has been established as an electron transport material for highly efficient inverted devices due to its high electron affinity and low temperature solution processability[8-9]. However, severe non-radiative recombination, defect accumulation and poor interfacial contact persisting at the perovskite (PVSK)/fullerene interface are widely reported[10-11]. Especially, PCBM exhibits certain limitations, including low electron mobility, a tendency to aggregate during film formation, and intrinsic thermal instability, which significantly restricts device performance and long-term stability[10,12].

The effective strategies to address the PVSK/PCBM interfacial issues involves inserting a functional interlayer between the perovskite and PCBM layers to address the inherent drawbacks arising from the physicochemical properties of the original interface and optimize interfacial contact quality. Many types of materials are used for interfacial regulation in PSCs, such as small organic molecules[8], polymers[13], ammonium salts[14], and so on[11]. For instance, Wei-Min Gu et al. develop a multifunctional interfacial regulation strategy to enhance the performance of perovskite solar cells by incorporating 2,2'-bipyridine-4, 4'-dicarbomethoxy (DMCBPy) between the perovskite and PCBM layers[8]. The 2,2'-bipyridine-moiety in DMCBPy can strongly anchor the undercoordinated ions on the perovskite surface through coordination interactions, regulate the interfacial energy level alignment, and reduce non-radiative recombination[8]. Dongyang Li et al. innovatively adopt a polymer (PY-IT) as an interfacial bridge between the perovskite and ETL, which reinforces PVSK/PCBM heterointerface bonding, reduces surface as well as bulk defects of PVSK[13]. Yifang Qi et al. employ ammonium salts to passivate perovskite films as well as improve the PVSK/PCBM interface, which reduces the surface roughness of perovskite films, facilitates charge transport, and suppresses PVSK/PCBM interfacial non-radiative recombination[14]. Furthermore, they point out that the ammonium salts can diffuse into gran boundaries and induce secondary grain growth ultimately forming perovskite films with larger grains and fewer defects[14]. In our previous work, the simple surface post-treatment with N-benzyloxycarbonyl-d-valine[15], ammonium

salts[16-17], is also attempted to improve the perovskite/PCBM interface. Although small-molecule, polymer and ionic interlayers for PVSK/PCBM modification have achieved substantial progress, most reported modifiers merely focus on passivating surface defects of perovskite, while little attention is paid to optimizing intimate contact between the two layers and mitigating PCBM aggregation via interfacial intercalation. In addition, most passivators possess an inadequate number of active sites, which limits their ability to achieve extensive and uniform defect passivation[17]. Specifically, intense π－π stacking triggers PCBM agglomeration during film fabrication and device operation, which creates discontinuous electron transport pathways, induces charge trapping, exacerbates interfacial recombination, and weakens perovskite－fullerene intermolecular coupling. It remains challenging to design novel interfacial materials that simultaneously achieve tight interface contact, inhibit PCBM aggregation and provide sufficient active sites for uniform defect passivation.

Steric hindrance molecular engineering has been verified to effectively suppress spontaneous PCBM self-aggregation for uniform heterointerfaces[18-19]. Cup-shaped macrocycles based on aromatic skeletons possess great potential to provide sufficient steric hindrance. Rational molecular design based on such aromatic macrocycles can simultaneously improve the dispersion state of PCBM and strengthen intermolecular coupling with fullerenes, remedying interfacial defects and improving charge transport performance. Calixarenes are a class of supramolecular macrocycles composed of phenol units linked by methylene bridges, featuring an aromatic framework and a conformationally flexible cavity. By virtue of their unique cavity structure, flexible derivatization sites, and excellent host-guest recognition abilities, they have been widely applied in fields such as ion-selective electrodes for catalysis, drug delivery, gelation, organic electronics, and sensors[20-21]. Recently, calixarene also been gradually introduced into PSCs field. Relying on host-guest interactions, relevant studies have achieved remarkable progress in ion immobilization and crystallization modulation[22-23]. Specifically, calixarenes can capture migrating ions and passivate defects, and also regulate the desolvation process to guide the oriented crystallization of high-quality perovskite films. Although calixarenes have proven effective in suppressing ion migration and passivating defects, their application in optimizing perovskite/PCBM heterointerfaces remains largely unexplored. Nevertheless, few existing interlayer materials with aromatic macrocyclic skeletons can simultaneously disperse PCBM molecules and enhance intermolecular interactions with fullerene cages[18,24]. In this regard, the exploration of calixarenes is expected to open up a new avenue for interfacial modification of perovskite/PCBM heterojunctions by utilizing macrocyclic host structural materials.

Here, a multifunctional interfacial modification strategy employing 4-sulfocalix[6]arene (SC6A) is proposed to overcome the PVSK/PCBM interface contact issues and inherent interfacial defects. SC6A features a cup-shaped macrocyclic aromatic scaffold , incorporating abundant sulfonic ($-SO_3H$) and hydroxyl groups (-OH). Such structural characteristics enable SC6A to achieve multi-site and omnidirectional coverage on perovskite surface, which simultaneously passivates various interfacial defects and suppresses undesirable carrier non-radiative recombination. Furthermore, the distinctive cavity of SC6A can form π－π interactions with PCBM, which helps regulate PCBM molecular distribution and enhance its dispersion. Such modification improves PCBM film uniformity, optimizes poor interfacial contact and promotes charge carrier transport. Benefiting from these synergistic functions, the optimized PSCs deliver a prominent PCE of 24.56%. Meanwhile, SC6A-modified devices obtain greatly enhanced long-term stability under nitrogen storage and thermal aging conditions compared with pristine devices.

2 Experiment

2.1 Materials

Methylammonium iodide (MAI, 99.5%), methylammonium bromide (MABr), formamidinium io-

dide (FAI), lead (II) bromide ($PbBr_2$), and bathocuproine (BCP, 99.0%) were procured from Xi'an Yuri Solar Co., Ltd. Aluminum oxide nanoparticles (Al_2O_3, 20 wt% in IPA) were obtained from Aladdin. Rubidium iodide (RbI, 99.9%), cesium iodide (CsI, 99.999%), and [2-(3,6-dimethoxy-9H-carbazol-9-yl) ethyl] phosphonic acid (MeO-2PACz, >98.0%) were supplied by TCI. Lead iodide (PbI_2, 99%) was purchased from Tianjin Damao Chemical Reagent Factory. [6, 6] -phenyl-C_{61}-butyric acid methyl ester (PCBM, 99.5%) was obtained from Nano-C. Solvents including N, N-dimethylformamide (DMF, 99.8%, super dry), dimethyl sulfoxide (DMSO, 99.8%, super dry), isopropanol (IPA, 99.8%, super dry), and chlorobenzene (CB, 99.8%, super dry), ethyl alcohol (98%) were sourced from J&K Scientific Ltd. Silver (Ag) was acquired from China New Metal Materials Technology Co., Ltd. 4-Sulfocalix [6]arene (SC6A, 95%) was obtained from Bide Pharmatech Co., Ltd. All other solvents and materials were procured from domestic suppliers without further purification.

2.2 Device Fabrication

To fabricate the devices, indium tin oxide (ITO)/glass were ultrasonically cleaned in sequence with detergent, distilled water, and IPA, each for 25 minutes. They were then dried with nitrogen and treated with UV-Ozone for 25 minutes. The substrates were subsequently transferred to a nitrogen-filled glove box filled with nitrogen, where a MeO-2PACz solution was deposited onto the ITO surface and dried at 100 °C for 10 minutes to form a thin hole transport layer. Next, an Al_2O_3 nanoplate dispersion was spin-coated onto the MeO-2PACz film at 4000 rpm for 30 seconds, followed by annealing at 100 °C for 10 minutes. The perovskite precursor was prepared by dissolving MABr, RbI, CsI, FAI, $PbBr_2$, and PbI_2 in a DMF:DMSO (4:1, v/v) mixture in stoichiometric proportions. This precursor was spin-coated at 4000 rpm for 30 seconds, with 100 μL of CB dropped onto the film 5 seconds before the end of the process. After annealing at 100 °C for 10 minutes, the active perovskite layer ($Rb_{0.05}Cs_{0.09}MA_{0.05}FA_{0.81}Pb(I_{0.95}Br_{0.05})_3$) was formed. Subsequently, SC6A solutions (dissolved in IPA) with different concentrations were spin-coated onto the perovskite film at 4000 rpm for 30 seconds. Next, a PCBM solution was spin-coated onto the modified perovskite layer at 4000 rpm for 30 seconds, followed by annealing at 90 °C for 30 minutes. Then, a BCP solution was spin-coated at 4000 rpm for 30 seconds as a buffer layer to enhance the interfacial contact between the PCBM layer and the silver (Ag) electrode. Finally, 100 nm Ag was thermally evaporated as the back electrode at a rate of 0.5-1 Å/s under a vacuum of 2-3×10^{-4} Pa.

2.3 Characterizations

The microstructural morphology of the films was examined by scanning electron microscopy (SEM) (FEI, Helios Nanolab 600i, USA). The surface potential of the films was measured by Kelvin probe force microscopy (KPFM) in tapping mode (Bruker, Multimode 8, Germany). Absorption spectra were recorded using a UV-vis spectrophotometer (PerkinElmer, Lambda 365, USA). X-ray diffraction (XRD) patterns were acquired using an X-ray diffractometer (Bruker, D8 Advance, Germany) with a Cu Kα radiation source operated at 40 kV and 44 mA. The current density-voltage (J–V) curves of PSCs were measured using a source meter (Keithley, 2400, USA) under AM 1.5G illumination at 100 mW cm^{-2} with solar simulator (AAA, Enlitech, SS-F5-3A, China). Light intensity was calibrated using astandard silicon solar cell. The transient photocurrents (TPC) and transient photovoltage (TPV) were measured by photo-electrochemical workstation (Zahner, Zennium pro, Germany).

3 Results and Discussion

3.1 SC6A–Perovskite Interaction Mechanism

SC6A features a cup-shaped macrocyclic aromatic scaffold, featuring dense arrays of sulfonic groups (-SO_3H) along its upper rim and hydroxyl groups (-OH) situated on the lower rim. The surface electrostatic potential map (ESP) (**Figure 1(a)**) reveals distinct positive and negative charge domains across the SC6A molecular surface. This unique polarity distribution provides abundant active sites for

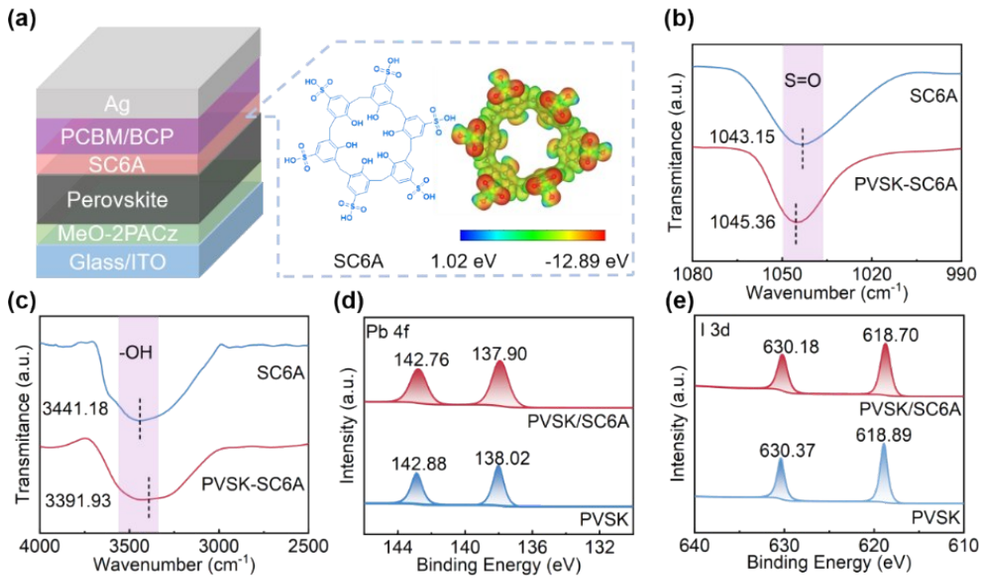

Figure 1 (a) Molecular structure of the SC6A molecule and its surface potential map. (b) FT-IR spectra of the S=O asymmetric stretching vibration and (c) -OH asymmetric stretching vibration for SC6A, PVSK-SC6A, and PVSK. XPS spectra of the (d) Pb 4f and (e) I 3d orbital for the PVSK and PVSK/SC6A films.

passivating defects with different electrical characteristics in perovskites, such as positively charged Pb interstitials and negatively charged iodine vacancies. ESP analysis indicates that the electron cloud is primarily concentrated on the $-SO_3H$ and -OH groups. Each sulfonic group_contains two S=O double bonds and exhibits strong electronegativity, suggesting that the $-SO_3H$ groups can coordinate with under-coordinated Pb^{2+} on the perovskite surface Lewis acid-base interactions, thereby achieving defect passivation[25-26]. In addition, the aromatic backbone and the introduction of multiple polar groups in the molecule may promote the formation of intermolecular π-π stacking and hydrogen bonds. Based on the above results SC6A is expected to act as an effective interfacial modifier for PVSK/PCBM heterojunction.

To further verify the interaction between SC6A and the perovskite, Fourier transform infrared (FT-IR) spectroscopy was performed. As shown in **Figure 1(b)**, the characteristic stretching vibration peak of the S=O group in the SC6A molecule is located at 1043.15 cm^{-1}[27-28], whereas this peak shifts to 1045.36 cm^{-1} in the SC6A-treated perovskite sample. This shift confirms the coordination between S=O and PbI_2. As shown in **Figure 1(c)**, the characteristic stretching vibration peak of -OH groups in SC6A appears at 3441.18 cm^{-1}, which shifts to 3391.93 cm^{-1} after SC6A treatment. It was speculated that -OH on SC6A could passivate the undercoordinated Pb^{2+} and iodide vacancy defects via coordination bond and electrostatic interaction according to Jiangzhao Chen's work[22]. We speculate that the -OH groups of calixarene can effectively passivate uncoordinated Pb^{2+} and iodide vacancy defects via coordination interactions and electrostatic interactions. The slight shift of the C=N stretching peak from 1720.72cm^{-1} to 1728.39 cm^{-1} (**Figure S1**) may relate with the formation hydrogen bonds between -OH groups of SC6A and FA^+ and I^- of PVSK film[22]. That hydrogen bonds have been confirmed that it will hold back the volatilization of FA^+ under thermal stress and inhibits the migration of FA^+ and I^-, benefiting for the stability of PVSK and devices[22].

To get more information about the SC6A interaction with perovskite, X-ray photoelectron spectroscopy (XPS) is carried out for PVSK film and PVSK/SC6A films. As shown in **Figure 1(d) and Figure 1 (e)**, the binding energies of Pb 4f shift from 138.02 eV and 142.88 eV for the pristine PVSK film to lower values of 137.90 eV and 142.76 eV for that of PVSK/SC6A film, while the XPS I 3d binding ener-

gies of the PVSK film (618.89 eV and 630.37 eV) exhibit a 0.19 eV downward shift in the PVSK/SC6A film. This reduction implies the enhancement of electron cloud density around Pb and I atoms upon SC6A adsorption on the PVSK surface, which can effectively inhibit the oxidation of I and the formation of interstitial I defect[29]. Simultaneously, the electron cloud enrichment strengthens the interaction between I^- and the lattice cations, enhances its binding stability at the lattice sites, and suppresses I^- desorption, thereby reducing the formation of VI defects[30]. From **Figure S2**, the shift of the N 1s peak of the perovskite film toward higher binding energy may be attributed to the hydrogen bond interaction between -OH on SC6A and FA^+.

3.2 Effect of SC6A Modification on Crystallinity and Morphology of Perovskite Films

In this work, a facile post-treatment processing is employed to introduce SC6A onto the perovskite film surface via spin-coating, achieving interfacial modification. For comparative analysis, the unmodified pristine perovskite film is designated as the control group, while the SC6A-modified film is referred to as the target group. X-ray diffraction (XRD) was performed to understand whether the surface passivation affected on the crystal structure of the perovskite films. As shown in **Figure 2(a)**, there are no obviously peak shifts and no additional diffraction peaks. Furthermore, the Ultraviolet-visible (UV-vis) absorption spectra of the control perovskite and SC6A-modified perovskite films show similar absorption properties (**Figure 2(b)**), all of which confirm that the introduction of SC6A does not alter the crystal phase of perovskite films and exerts no adverse effects on the optoelectronic properties of bulk perovskite films. Notably, the intensity of the (100) diffraction peak increases in the experimental group, and the intensity ratio of the (100) to (110) diffraction peaks rise from 1.04 to 1.69. This indicates that SC6A modification promotes the preferred orientation of the (100) lattice plane, which helps reduce trap states and thereby facilitates charge carrier transport across the perovskite lattice[31].

The surface morphology and structural characteristics of the perovskite films were characterized using scanning electron microscopy (SEM) and atomic force microscopy (AFM). The SEM images are presented in **Figure 2(c) and 2(d)**, while the AFM images are shown in **Figure 2(e) and 2(f)**. The top-view SEM image of the control film (**Figure 2(c)**) reveals numerous deep pinholes on the surface. These defects not only lead to poor interfacial contact be-

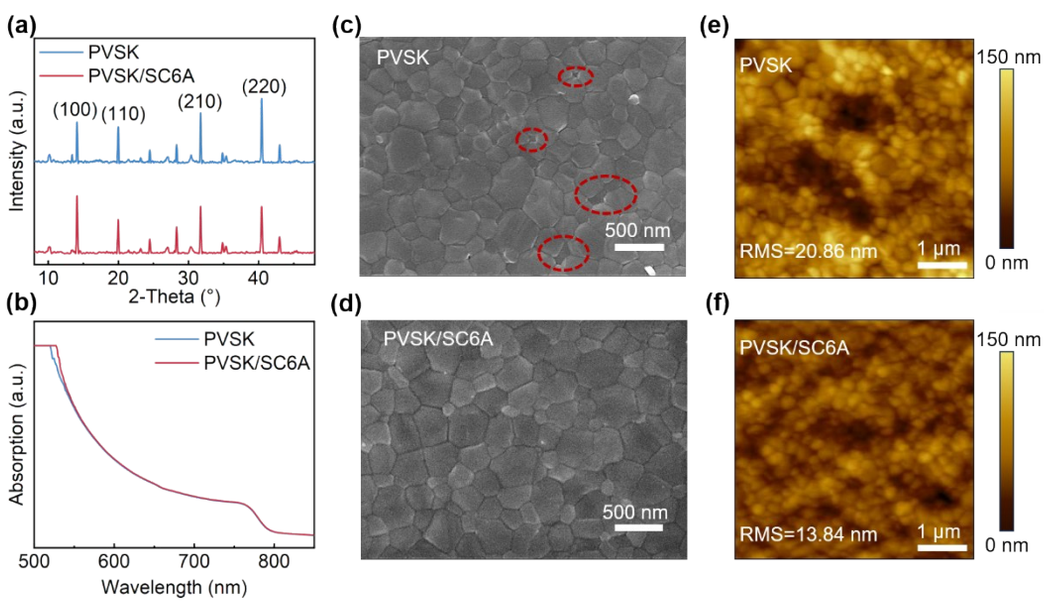

Figure 2 (a) UV-vis of the PVSK and PVSK/SC6A films. (b) XRD patterns of the PVSK and PVSK/SC6A films. (c) and (d) Top-view SEM images of PVSK film and PVSK/SC6A films. (e) and (f) AFM surface images (5 μm×5 μm) of PVSK films and PVSK/SC6A films.

tween the perovskite layer and the overlying PCBM electron transport layer but also serve as pathways for moisture and oxygen penetration, thereby exacerbating non-radiative recombination losses and accelerating film degradation[32]. After SC6A modification, the surface morphology of the target film is markedly improved (**Figure 2(d)**), with a substantial reduction in pinhole density and a more compact, uniform film structure. AFM measurements indicate that the root-mean-square (RMS) roughness decreases from 20.86 nm for the control film to 13.84 nm after SC6A treatment, demonstrating that SC6A modification effectively reduces surface roughness and enhances film smoothness. A smoother surface facilitates improved interface contact and charge transport[18].

Cross-sectional SEM images (**Figure S3**, Supporting Information) further illustrate the structural differences between the films. The control film exhibits a highly undulating upper interface with abundant fragmented grains distributed both laterally and vertically, along with loose and pronounced grain boundaries. In contrast, SC6A effectively fills the grain boundary voids and repairs surface pinholes, resulting in a uniform and dense film structure. This treatment significantly reduces the number of lateral grain boundaries and renders the upper interface of the perovskite film considerably flatter and smoother. Such an optimized interfacial structure facilitates the uniform deposition of the subsequent PCBM layer, effectively suppresses interfacial carrier recombination, and lays a solid foundation for enhancing the overall photovoltaic performance and stability of the device[18,33].

3.3 PCBM Immobilization by SC6A: Improving Film Uniformity and Interfacial Contact.

To investigate the impact of SC6A modification on the film formation quality of the overlying PCBM layer, atomic force microscopy (AFM) was performed on PVSK/PCBM and PVSK/SC6A/PCBM composite films. The AFM results (**Figure 3(a) and 3(b)**) reveal that following SC6A modification, the root-mean-square (RMS) roughness of the PCBM film is significantly reduced from 11.34 nm in the control group to 9.41 nm in the target group. This indicates that SC6A modification effectively improves the uniformity of the PCBM film and reduces surface defects[33-34].

The scanning Kelvin probe force microscopy (SKPFM) was used to measure the PVSK films before and after SC6A treatment (**Figure S4**). After SC6A modification, the average surface potential of the PVSK films was significantly increased. This enhancement may be attributed to surface passivation primarily occurring through coordination between the $-SO_3H$ and -OH groups with positively charged trap states, which reduces surface charge density and induces Fermi level shifting[18,35]. Meanwhile, the potential fluctuation amplitude decreases from 22.02 to 15.47 mV. This reduction of the potential fluctuation amplitude indicates a more uniform potential distribution. It is speculated that these improvements may be caused by the combined effects of the following factors: The $-SO_3H$ and -OH groups coordination effectively repairs the relevant defects, eliminates the defect states generated at the defect sites due to surface charge imbalance, and the $-SO_3H$ and -OH groups on the edge generate strong interface dipoles[18,24,35].

The corresponding dipole optimizes energy-level alignment at the PVSK/PCBM interface, promoting efficient electron extraction and suppressing non-radiative recombination[35-37]. To explore how SC6A affects the energy level alignment and charge extraction at the PVSK/PCBM interface, SKPFM was also performed on the corresponding heterostructures. The SKPFM results for the PCBM films (Figure 3(d) and 3(e)) show that after SC6A modification, the average surface potential of the PCBM film is significantly enhanced[35]. These dipoles enable nearly perfect alignment between the conduction band minimum (CBM) of perovskite and the lowest unoccupied molecular orbital (LUMO) of PCBM, thereby achieving efficient and barrier-free electron extraction[30,35].

The potential fluctuation amplitude decreases from 18.39 mV to 12.63 mV (**Figure 3(c)**). The reduction in potential fluctuation amplitude indicates a more uniform surface potential distribution. This

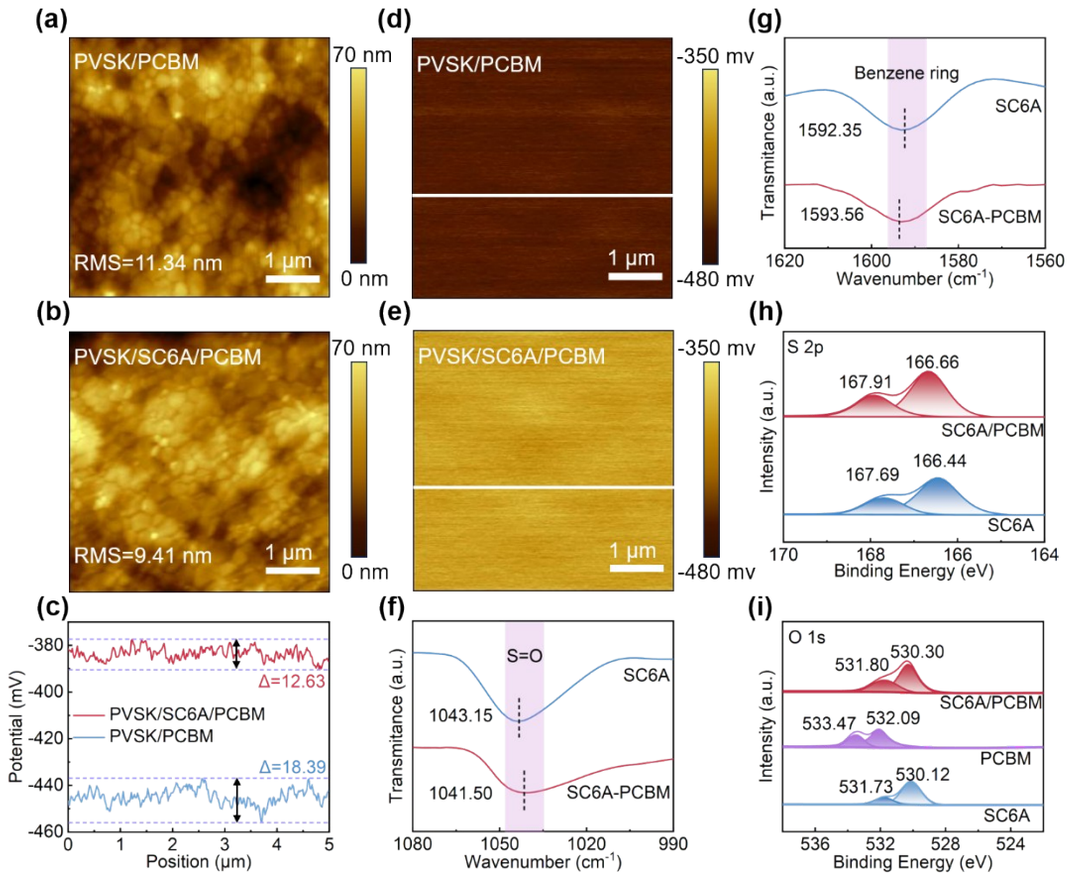

Figure 3 (a) and (b) AFM surface images (5 μm×5 μm) of PCBM and SC6A/PCBM films. (c) Surface potentials corresponding to the two white lines in (d) and (e). (d) and (e) SKPFM results of PCBM and SC6A/PCBM films. (f) FT-IR spectra of asymmetric stretching of S=O for SC6A and SC6A/PCBM films. (g) FT-IR spectra of asymmetric stretching of benzene ring for SC6Aand SC6A/PCBM films. (h) XPS spectra of the S 2p orbital of the SC6A and SC6A/PCBM films. (i) XPS spectra of the O 1s orbital of the SC6A, PCBM and SC6A/PCBM films.

phenomenon can be attributed to the anchoring effect of the SC6A macrocyclic cavity on PCBM molecules, which effectively improves the dispersion of PCBM and thus provides a flat, uniform interfacial channel for charge transport[12,19,35]. The high-quality PCBM film significantly promotes charge extraction efficiency and minimizes carrier recombination losses at the perovskite/PCBM interface, which is considered one of the key factors in enhancing the performance of inverted perovskite solar cells[19].

To explore the enhancement mechanism of SC6A on the film-forming properties of PCBM, we systematically studied the intermolecular interactions between these two materials. FTIR spectroscopy analysis (**Figure 3(f)**) reveals that the characteristic stretching vibration peak corresponding to the S=O in SC6A undergoes a shift from 1043.15 cm^{-1} to 1041.50 cm^{-1}. This subtle shift implies a potential electronic interaction between the -SO_3H groups of SC6A and PCBM. The oxygen atoms of the -SO_3H groups in SC6A contain lone electron pairs and serve as Lewis bases to donate electrons. As a typical electron acceptor, PCBM tends to capture free electrons. The sulfonic groups form positively charged dipoles after losing electrons, whereas PCBM becomes negatively charged upon accepting electrons, which facilitates the formation of dipole-dipole interactions between the two substances[34-35,38]. Meanwhile, the characteristic peak of hydroxyl groups for SC6A shifts from 3441.18 cm^{-1} to 3428.18 cm^{-1}. (Figure S5, Supporting Information), and the benzene ring characteristic peak moves from 1592.35 cm^{-1} to 1593.56 cm^{-1} (**Figure 3(g)**). These results indicate the possible existence of hydrogen

bonding and π-π interactions between SC6A and PCBM[24,39].

XPS results provide further evidence of the interaction between SC6A and PCBM. In the S 2p XPS spectrum of SC6A (**Figure 3(h)**), the characteristic peaks of the sulfur atoms in the sulfonic groups (S $2p_{3/2}$ and S $2p_{1/2}$) shift slightly from 166.44 eV and 167.69 eV to 166.66 eV and 167.91 eV, respectively. This indicates an alteration in the electronic environment of the sulfur atoms, confirming their participation in the interaction with PCBM. Furthermore, distinct shifts are observed in the O 1s orbitals of both PCBM and SC6A (corresponding to the oxygen atoms in the sulfonic and hydroxyl groups) (**Figure 3(i)**), which further validates the existence of intermolecular interactions between the two species.

Based on these characterization results, it is hypothesized that the interaction between SC6A and PCBM is driven by a synergy of multiple non-covalent bonds. On one hand, strong hydrogen bonding is formed between the PCBM molecules and the hydroxyl groups (-OH) of SC6A. On the other hand, the aromatic ring structures in both molecules facilitate π-π stacking interactions. These forces, assisted by intermolecular dipole-dipole interactions, collectively enhance the binding affinity between SC6A and PCBM. This robust interaction significantly improves the film-forming quality of PCBM, providing substantial support for the construction of efficient and stable interfacial electron transport channels.

3.4 Effects of SC6A on Device Photovoltaic Performance

To directly demonstrate the positive impact of SC6A on device performance, inverted PSCs are fabricated both with and without the SC6A post-treatment. The current density-voltage (*J*–*V*) characteristics of these devices are measured under standard one-sun illumination conditions (AM 1.5 G, 100 mW cm^{-2}). SC6A is introduced upon the perovskite thin films using a solution method, with its thickness adjusted by varying the concentration of SC6A solution. As detailed in Table S1, the device power conversion efficiency (PCE) exhibits a clear increasing trend with increasing SC6A concentration, reaching an optimal value at 0.05 mg/mL, where the champion device achieves the highest PCE of 24.56%. When the concentration is further increased beyond 0.05 mg/mL, the device PCE slightly decreases, indicating the existence of an optimal concentration. At this optimal concentration, SC6A effectively passivates defects, suppresses non-radiative recombination, and optimizes interfacial contact. However, excessive SC6A layers may introduce additional interfacial resistance, thereby hindering charge transport. Therefore, we fix that optimal concentration to prepare the devices for further comparative studies. The *J*–*V* characteristics for both the control and SC6A devices are shown in Figure 4(a). The best control device exhibits a maximum PCE of 22.54 %, with V_{oc} of 1.126 V, short-circuit current density (J_{sc}) of 25.56 mA cm^{-2} and fill factor (*FF*) of 78.30 %. In contrast, the best SC6A device shows a notable enhancement in device performance compared with that of control one, resulting in a relatively higher PCE of 24.56 %, with V_{oc} of 1.148 V, J_{sc} of 26.06 mA cm^{-2} and higher *FF* of 82.10 %.

The EQE spectra of typical control and SC6A devices are shown in **Figure 4(b)**. The introduction of SC6A has resulted in an improvement in the EQE in the 600-800 nm band range, correspondingly leading to an increased J_{sc}. This enhancement is consistent with the improving trend in J_{sc}. The increase in J_{sc} can be attributed to enhanced light absorption, improved charge transfer, and more efficient charge extraction. Additionally, SC6A acts as an efficient passivator and interface modifier, which may benefit the reduction of the hysteresis of the devices. Figure 4(c) presents the *J*–*V* characteristics of both control and SC6A devices based on different voltage scanning directions. The detailed devices performance parameters are summarized in **Table S2**. Hysteresis index (HI) is also calculated according to Equation (1)[40].

$$HI = \frac{PCE^{-} - PCE^{+}}{PCE^{-}} \quad (1)$$

Here, PCE^{+} and PCE^{-} are the PCE obtained in the forward and reverse scanning directions, respec-

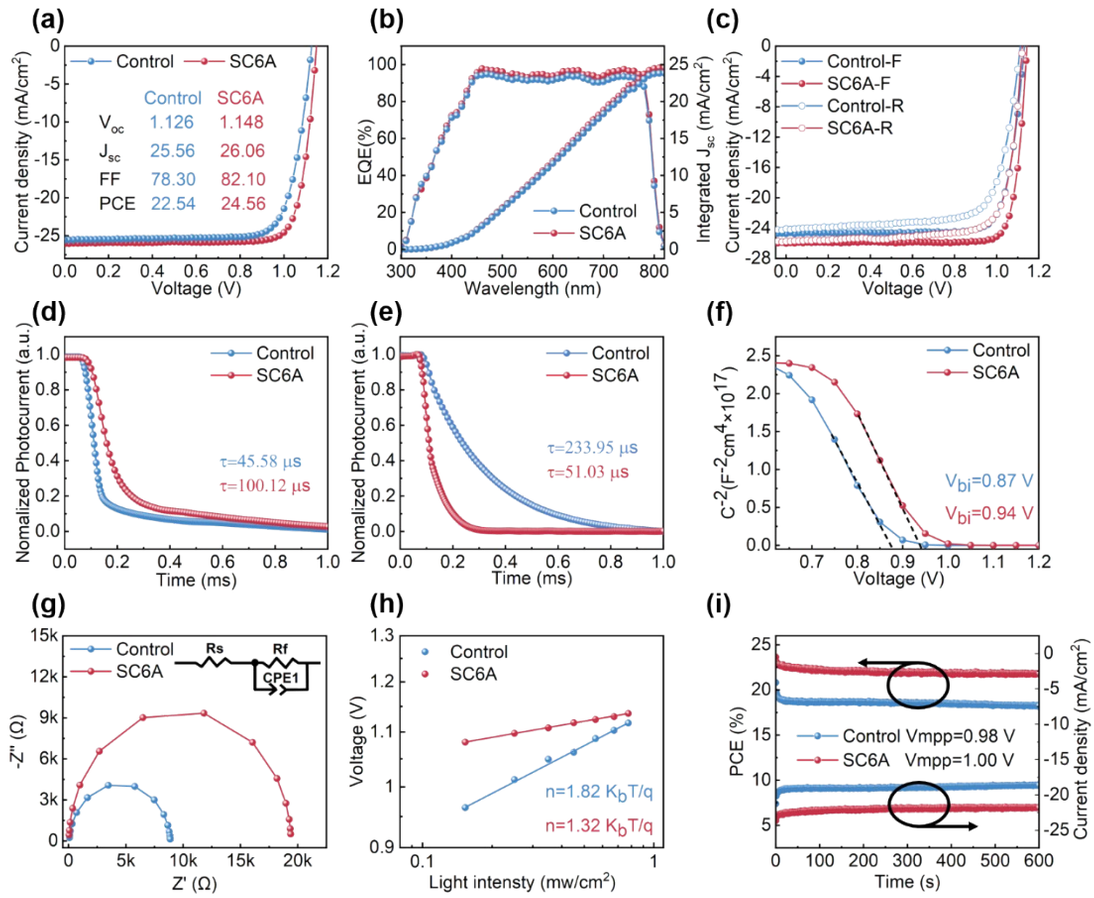

Figure 4 (a) *J*–*V* characteristics of optimal control and SC6A devices. (b) EQE spectra with corresponding integrated current densities for control and SC6A devices. (c) Forward and reverse scan *J*–*V* curves of control and SC6A devices. (d) TPV of control and SC6A devices. (e) TPC of control and SC6A devices. (f) Mott-Schottky plots of the control and SC6A devices. (g) Nyquist plots of the control and SC6A devices. (h) *Voc* varies with light intensity. (i) Steady-state power output for control and SC6A devices.

tively. The calculated HI of control and SC6A devices is 7.24% and 3.89%, respectively. Hysteresis is primarily caused by defects in the devices as reported previously[41]. Therefore, the HI reduction can be attributed to the elimination of defects by the SC6A introduction.

To elucidate the impact of SC6A modification on carrier dynamics, transient photovoltage (TPV) and transient photocurrent (TPC) measurements were conducted. The TPV and TPC curves of the control and SC6A devices are shown in **Figure 4(d) and Figure 4 (e)**. Both curves conformed to double exponential characteristics, and the detailed fitting results are referred to **Table S3 and Table S4** for TPV and TPC. TPV reveals a significant extension of the carrier recombination lifetime from 48.58 μs for the control device to 100.12 μs for the SC6A-modified device. This result clearly indicates that SC6A effectively passivate defect states at the perovskite surface and the perovskite/PCBM interface, thereby substantially suppressing non-radiative recombination. The superior passivation achieved by SC6A is consistent with the observed enhancement in V_{oc}. TPC shows accelerated carrier extraction, with decreasing from 233.95 μs (control) to 51.03 μs (SC6A), indicating that SC6A interlayer optimizes energy level alignment at the interface and forms efficient extraction pathways from the PVSK to PCBM[32,42].

The built-in potential (V_{bi}) derived from the Mott-Schottky capacitance analysis (Figure 4(f)) increases from 0.87 V to 0.94 V after SC6A introduction. This elevated V_{bi} can be attributed to the effective defect passivation at the PVSK/PCBM interface by SC6A, which suppresses non-radiative recombina-

tion and reduces voltage loss, enhancing V_{oc}. Electrochemical impedance spectroscopy (EIS) measurements were performed under dark conditions with a bias voltage of 0.85 V. The Nyquist plots of the devices are shown in **Figure 4(g)** and fitted using the equivalent circuit shown in the inset, with fitting results summarized in **Table S5**. The recombination resistance (R_{rec}) of SC6A devices increases from 8813 to 19255Ω, providing additional evidence for suppressed carrier recombination[29].

A key parameter for analyzing the voltage–light intensity dependence is the ideal diode factor (n), which can be calculated by the formula (2)

$$n = K_b T/q \times \Delta V_{oc}/\Delta \ln J_L \quad (2)$$

Here, q is the elementary charge, and J_L refers to the photogenerated current density[17]. When the ideal diode factor n is close to 2, it indicates that trap-mediated Shockley-Read-Hall recombination dominates the recombination process. The lower ideal factor (n = 1.32) of SC6A device compared to that of the control device (n = 1.82) (**Figure 4(h)**), suggesting a significant reduction in energy loss induced by trap-assisted Shockley – Read – Hall recombination. This further highlights the suppressed defect-assisted recombination and improved interfacial contact. In summary, SC6A effectively suppresses recombination through superior defect passivation and accelerates charge extraction by optimizing interfacial contact, thereby enabling higher device performance.

The stable output PCE (PCE_{mpp}) and current density (J_{mpp}) of the device running at the maximum power point (MPP) under continuous illumination (AM 1.5G, 100 mW cm^{-2}) are also measured. The PCE_{mpp} and J_{mpp} of the SC6A device are 23.75 % and 23.75 mA cm^{-2}, which is higher than those of the control device (PCE_{mpp} 20.83 % and J_{mpp} 21.25 mA cm^{-2}) (**Figure 4(i)**). It indicates that the maximum power point output performance of the SC6A device has greater power and better stability.

3.5 Impact of SC6A on Device Stability

Stability represents another critical criterion for the practical application of perovskite photovoltaic technology. Thus, we systematically tracked the stability of the SC6A-modified target devices and the unmodified control devices to evaluate their long-term storage stability and thermal stability, with all tested devices being unencapsulated. For better comparison, linear fitting was applied to the stability curves. The unencapsulated devices stored in a nitrogen-filled glove box at room temperature were monitored for over 1500 hours (**Figure 5(a)**). The control devices retained 80% of their initial efficiency, whereas the SC6A-modified devices exhibited significantly improved storage stability, with a retention of 93% of their initial PCE. This enhancement is attributed to the suppressed non-radiative recombination and optimized interfacial contact, which thus slow down device degradation.

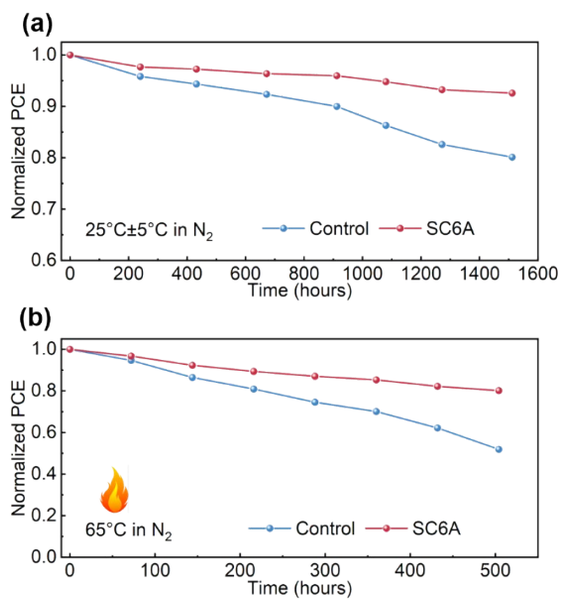

Figure 5 (a) Stability of the control and SC6A PSCs under various conditions: (a) In N_2 at room temperature; (b) In N_2 at 65 °C.

Thermal stability is essential for the long-term operational stability of the devices. Therefore, we placed the devices on a hot plate in a N_2-filled glove box at 65 °C to assess their thermal stability (**Figure 5(b)**). After 500 hours of thermal aging, the SC6A-modified devices still retained 80% of their initial PCE, which was superior to that of the control devices (52%).

4 Conclusion

In summary, a multifunctional interfacial modi-

fication strategy using 4-sulfocalix[6]arene (SC6A) was proposed to solve severe non-radiative recombination and poor interfacial contact issues at PVSK/PCBM heterojunction. With cup-shaped macrocyclic architecture and abundant functional groups, SC6A achieves multi-site omnidirectional defect passivation to suppress non-radiative recombination. Its cavity also immobilizes PCBM molecules to improve their dispersion, which in turn enhances film uniformity and interfacial contact. Benefiting from these synergistic effects, the optimized PSCs obtain a high PCE of 24.56%, and retain 93% efficiency after 1500 h N_2 storage and 80% efficiency after 500 h thermal aging. This work demonstrates that calixarene molecules are promising interfacial modifiers for high-performance and stable inverted PSCs, providing a feasible molecular design strategy for optimizing perovskite/electron transport layer interfaces.

References:

[1] VICTORIA M, HAEGEL N, PETERS I M, *et al*. Solar photovoltaics is ready to power a sustainable future [J]. *Joule*, 2021, 5(5): 1041-1056.

[2] COTFAS D T, SERA D, Kaplani E, *et al*. Advancements in photovoltaic cell and system technologies [J]. *Int. J. Photoenergy*, 2019, 2019: 1-2.

[3] LI D, SUN F L, LIANG C J, *et al*. Effective approach for reducing the migration of ions and improving the stability of organic-inorganic perovskite solar cells [J]. *J. Alloys Compd.*, 2018, 741: 489-494.

[4] 侯昱,刘金龙,许鹤,等. 多功能乳清酸钝化协助制备高效稳定的钙钛矿太阳能电池[J]. 发光学报, 2024, 45(8): 1364-1370.
HOU X, LIU J L, XU H, *et al*. Multifunctional orotic acid passivation for efficient and stable perovskite solar cells [J]. *Chin. J. Lumin.*, 2024,45(8): 1364-1370. (in Chinese)

[5] JIANG Q, ZHU K. Rapid advances enabling high-performance inverted perovskite solar cells [J]. *Nat. Rev. Mater.*, 2024, 9(6): 399-419.

[6] LIN X S, CUI D Y, LUO X H , *et al*. Efficiency progress of inverted perovskite solar cells [J]. *Energy Environ. Sci.*, 2020.

[7] YAN N, FANG Z M, DAI Z H, *et al*. Buried interface-the key issues for high performance inverted perovskite solar cells [J]. *Adv. Funct. Mater.*, 2024, 34(22): 2314039.

[8] GU W M, ZHAO M M, WANG Q, *et al*. Regulating perovskite/PCBM interface for highly efficient and stable inverted perovskite solar cells [J]. *Chem. Eng. J.*, 2025, 509: 161237.

[9] ZHANG X, ZHANG J, LIU D T, *et al*. Functionalized fullerene: a key driver for high performance inverted perovskite solar cell [J]. *J. Energy Chem.*, 2025, 111: 30-50.

[10] WU J C, ZHANG J Y, WANG L Y, *et al*. Diastereomeric fullerene composite engineering for enhanced perovskite solar cells [J]. *J. Am. Chem. Soc.*, 2025, 147(35): 32045-32053.

[11] WANG H, LIU C T, XU R D, *et al*. Upper interface engineering between perovskite and electron transport layer toward efficient and stable inverted perovskite solar cells [J]. *Adv. Mater.*, 2026, 38(5): e13633.

[12] LIANG Z, XU H F, HUANG Z D, *et al*. Suppression of PCBM dimer formation in inverted perovskite solar cells [J]. *Nat. Mater.*, 2026, 25(2): 267-274.

[13] LI D Y, HUANG Y L, MA R J, *et al*. Surface regulation with polymerized small molecular acceptor towards efficient inverted perovskite solar cells [J]. *Adv. Energy Mater.*, 2023, 13(18): 2204247.

[14] QI Y F, AGUINAGA J, TERLIER T, *et al*. Effective selection and targeted passivation for different defect types by ammonium salts in perovskite solar cells [J]. *Adv. Energy Mater.*, 2025, 15(42): e00678.

[15] XIONG J, LIU N H, HU X T, *et al*. Bulk restructure of perovskite films via surface passivation for high-performance solar cells [J]. *Adv. Energy Mater.*, 2022, 12(33): 2201787.

[16] DAI J Q, XIONG J, LIU N H, *et al*. Synergistic dual-interface modification strategy for highly reproducible and efficient PTAA-based inverted perovskite solar cells [J]. *Chem. Eng. J.*, 2023, 453: 139988.

[17] XIONG J, DAI Z J, ZHAN S P, *et al*. Multifunctional passivation strategy based on tetraoctylammonium bromide for effi-

cient inverted perovskite solar cells [J]. *Nano Energy*, 2021, 84: 105882.

[18] LIAO Y Y, ZHANG J K, ZHU M Z, *et al*. Coordination/π-π stacking synergistic strategy: regulating interface defects and charge transport to enhance the performance of tin-lead perovskite solar cells [J]. *Adv. Funct. Mater.*, 2026, 36(30): e24337.

[19] HE Q Q, LI R Y, ZHANG T, *et al*. Simultaneous solvent and interface engineering of electron transport layer for efficient and stable perovskite solar cells [J]. *Nano Lett.*, 2026, 26(10): 3398-3406.

[20] SHARMA V S, VISHWAKARMA V K, SHRIVASTAV P S, *et al*. Calixarene functionalized supramolecular liquid crystals and their diverse applications [J]. *ACS Omega*, 2022, 7(50): 45752-45796.

[21] WOJACZYŃSKA E, OSTROWSKA M, LOWER M, *et al*. Recent advances in synthesis and applications of calixarene derivatives endowed with anticancer activity [J]. *Molecules*, 2024, 29(17): 4240.

[22] HE D M, MA D Q, ZHANG J J, *et al*. Universal ion migration suppression strategy based on supramolecular host–guest interaction for high-performance perovskite solar cells [J]. *Adv. Mater.*, 2025, 37(33): 2505115.

[23] LIU X Y, XIE J, ZHOU Z R, *et al*. Reproducible fabrication of perovskite photovoltaics via supramolecule confinement growth [J]. *Nano-Micro Lett.*, 2026, 18(1): 67.

[24] LI X Y, XU Z W, ZHAO R M, *et al*. Multifunctional interfacial molecular bridging strategy enables efficient and stable inverted perovskite solar cells [J]. *Adv. Mater.*, 2025, 37(34): 2508352.

[25] YI F X, GUO Q Y, H W, *et al*. Trimethyl ammonium-assisted interfacial modification for efficient and stable wide-band-gap perovskite solar Cells [J]. *Energy Technol.*, 2024, 12(1): 2300780.

[26] CAI W L, WANG J G, ZHU X Y, *et al*. In situ dual-region selective anchoring of zwitterionic gel enables efficient and mechanically durable flexible perovskite solar cell [J]. *Adv. Energy Mater.*, 2026, 16(7): e05869.

[27] YANG G Y, YIN Y F, DONG K W, *et al*. Realizing uniform defect passivation via self-polymerization of benzenesulfonate molecules in perovskite photovoltaics [J]. *Adv. Mater.*, 2025, 37(29): 2503435.

[28] AZIGULI H, LU T, ZHAO H Y*et al*. Multifunctional hydroxylamine-o-sulfonic acid as additives for highly efficient and stable perovskite solar cells [J]. *Sol. RRL*, 2024, 8(12): 2400253.

[29] ZUO Y Q, WANG G, PU Y W, *et al*. Gemini quaternary ammonium salt-enabled efficient interface and bulk engineering for inverted perovskite solar cells [J]. *J. Energy Chem.*, 2026, 118: 245-258.

[30] HE Z, XIONG J, ZUO Y Q, *et al*. Efficient targeted regulation of the interfaces and bulk in inverted perovskite solar cells with a [*closo*-$B_{12}H_{12}$]$^{2-}$-based derivative [J]. *Adv. Mater.*, 2025, 37(5): 2414155.

[31] LI B, SHEN T, YUN S N. Recent progress of crystal orientation engineering in halide perovskite photovoltaics [J]. *Mater. Horiz.*, 2023, 10(1): 13-40.

[32] PU Y W, LIANG Y C, HE Zhen, *et al*. Spatial self-assembled ionic bridge strategy for overcoming perovskite/PCBM heterojunction issues in inverted perovskite solar cell [J]. *Adv. Funct. Mater.*, 2026, 36(35): e31831.

[33] LI M B, YANG Y H, LI S, *et al*. A molecularly engineered electron-selective self-assembled monolayer enhances quasi-fermi level splitting in inverted perovskite solar cells [J]. *Nat Energy*, 2026.

[34] GONG C, LI H Y, XU Z Y, *et al*. Efficient and stable inverted perovskite solar cells enabled by homogenized PCBM with enhanced electron transport [J]. *Nat. Commun*, 2024, 15(1): 9154.

[35] CHEN X, XU P, WANG Q, *et al*. Supramolecular cavity confinement inducing ordered C_{60} assembly and Suppressed interfacial non-radiative recombination for efficient and scalable perovskite solar cells [J]. *Adv. Funct. Mater.*, 2026, 36(32): e30794.

[36] XU P, CHEN X, HUI W, *et al*. Retarding the growth kinetics of chemical bath deposited nickel oxide films for efficient inverted perovskite solar cells and minimodules [J]. *Adv. Mater.*, 2025, 37(29): 2505087.

[37] JIAO B X, YE Y R, TAN L G, *et al*. Realizing stable perovskite solar cells with efficiency exceeding 25.6% through crystallization kinetics and spatial orientation regulation [J]. *Adv. Mater.*, 2024, 36(25): 2313673.

[38] WANG G, WANG D, CHANG J, *et al*. Dipolar interlayers in perovskite solar cells [J]. *Solar RRL*, 2023, 7(20): 2300481.

[39] LI Z J, WANG K, LI R, *et al*. Interfacial energetics reconstruction via bridging engineering for efficient inverted perovskite solar cells and modules [J]. *Angew. Chem. Int. Ed.*, 2026, 65(22): e9286497.

[40] HABISREUTINGER S N, NOEL N K, SNAITH H J. Hysteresis index: a figure without merit for quantifying hysteresis in

perovskite solar cells [J]. *ACS Energy Lett.*, 2018, 3(10): 2472-2476.

[41] LIU N H, XIONG J, HE Z, *et al*. Multifunctional anti-corrosive interface modification for inverted perovskite solar cells [J]. *Adv. Energy Mater.*, 2023, 13(20): 2300025.

[42] YANG J W, WANG Q, HUI W, *et al*. Crystal phase and band edge modulation of MA- and Br-free CsFA-based perovskites for efficient inverted solar cells and minimodules [J]. *Energy Environ. Sci*, 2025, 18(4): 1732-1744.

杨雪珂(2000-),女,河南开封人,硕士研究生,2024年于周口师范学院获得学士学位,主要从事钙钛矿太阳能电池器件的研究。

E-mail:3513684599@qq.com

熊健(1984-),男,湖南常德人,博士,教授,博士生导师,2015年毕业于中南大学物理与电子学院获得博士学位,主要从事有机太阳能电池、钙钛矿太阳能电池器件的研究。

E-mail:xiongjiankyxx@163.com